High cycle fatigue life prediction of laser additive manufactured stainless steel: A machine learning approach

Meng Zhang[1,2], Chen-Nan Sun[3], Xiang Zhang[4], Phoi Chin Goh[2], Jun Wei[3], David Hardacre[2], Hua Li[1*]

[1] *Singapore Centre for 3D Printing, School of Mechanical and Aerospace Engineering, Nanyang Technological University, 50 Nanyang Avenue, Singapore 639798*
[2] *Lloyd's Register Singapore Pte Ltd, 1 Fusionopolis Place, #09-11 Galaxis, Singapore 138522*
[3] *Singapore Institute of Manufacturing Technology, A*STAR, 73 Nanyang Drive, Singapore 637662*
[4] *Faculty of Engineering, Environment & Computing, Coventry University, Coventry CV1 5FB, UK*

**Corresponding author: lihua@ntu.edu.sg*

Abstract

Variations in the high cycle fatigue response of laser powder bed fusion materials can be caused by the choice of processing and post-processing strategies. The numerous influencing factors arising from the process demand an effective and unified approach to fatigue property assessment. This work examines the use of a neuro-fuzzy-based machine learning method for predicting the high cycle fatigue life of laser powder bed fusion stainless steel 316L. A dataset, consisting of fatigue life data for samples subjected to varying processing conditions (laser power, scan speed and layer thickness), post-processing treatments (annealing and hot isostatic pressing) and cyclic stresses, was constructed for simulating a complex nonlinear input-output environment. The associated fracture mechanisms, including the modes of crack initiation and deformation, were characterised. Two models, by employing the processing/post-processing parameters and the static tensile properties respectively as the inputs, were developed from the training data. Despite the diverse fatigue and fracture properties, the models demonstrated good prediction accuracy when checked against the test data, and the computationally-derived fuzzy rules agree well with understanding of the fracture mechanisms. Direct application of the model to literature results, however, yielded a range of prediction accuracies because of the variability in the reported data. Retraining the model by incorporating the literature results into the dataset led to improved modelling performance.

Keywords: Fatigue, fracture, neuro-fuzzy modelling, stainless steel 316L, additive manufacturing

1. Introduction

Recent progress in additive manufacturing (AM) has encouraged the use of the technology beyond rapid prototyping to direct manufacture of functional parts [1-3]. Comparing with traditional production techniques, AM systems are associated with added complexities because of the wide range of processing variables [4]. The laser powder bed fusion (L-PBF) process, for example, is associated

with a large number of adjustable parameters such as the laser power, scan speed, layer thickness and hatch strategies [5-7]. Variations in these parameters can lead to different thermal behaviours [8], microstructure and defect features [9]. High cycle fatigue is among the material properties that is very sensitive to processing because of the strong influence of microstructure and defects on crack initiation [10]. The significant variability in the S-N properties of L-PBF alloy as a function of processing, thermal treatment and surface finish had been demonstrated in a review of literature fatigue data by Li et al. [11]. Material discontinuities in the form of lack of fusion defects had been reported to cause premature crack initiations in many L-PBF alloys [12-14]. With an increase in defect density, the interaction among closely-spaced defects can lead to accelerated crack propagation and rapid rupture [15]. As defect size reduces with better process control, the effects of the hierarchical microstructural features, e.g. directional grains and melt pools at the macro-scale, and ultrafine sub-grains, porosities and inclusions at the micro-scale [16, 17], become relevant.

As highlighted by Nicoletto [18], the complex processing environment and failure behaviour make fatigue property assessment of L-PBF parts inherently challenging. Implementation of mechanistic fatigue model has seen limited progress because of the diverse L-PBF defects that impact the material behaviour. For instance, defect-based constitutive models often assume negligible effects of microstructure or homogenous microstructure arrangement [19]. But such assumptions are not valid, as the steep temperature gradient during L-PBF processing is known to generate highly anisotropic and heterogeneous microstructures [20]. Microstructure-based models [21, 22] can be employed, but the characterisation of microstructural features, e.g. grain and inclusion sizes, is not easy because of significant part-to-part and built-to-built variabilities [23] and the influence of processing on microstructure formation. Traditional phenomenological models, e.g. the √area model by Murakami and the Kitagawa-Takahashi diagram with El Haddad formulation, had been adapted for correlating L-PBF defects with fatigue strength [13, 24]. However, they demonstrated limited applicability that is contingent on the processing and post-processing strategies or defect conditions. As existing models do not contain L-PBF-related factors, they cannot be directly applied for mapping the process-property relationships. The use of separate models for treating the process-structure and structure-property relationships [25] is associated with increased computational cost and various sources of model uncertainties [26].

Data-driven approach utilising the design of experiment technique had also been studied, where the process and fatigue life relationship of L-PBF stainless steel 316L was examined for a two-factor system [27]. However, despite the small process window tested, the fatigue failure behaviour was too complex to be effectively modelled using first- or second-order regression equations. Moreover, models constructed using these methods often have limited generalisation capability as the systematic experimental design prevents the adaptation of data from the literature or public domain [28].

Machine learning techniques are effective alternatives for solving engineering problems as they are capable of recognising patterns in complex data [29]. Advanced data science algorithms such as the artificial neural network had been used for mapping the process-property relationships of various manufacturing processes, e.g. classification of welding defects for a three-input system [30] and tensile strength prediction of rolled steel plates for a six-input system [31]. The strong versatility may be leveraged for addressing the intricacies of L-PBF.

In particular, the adaptive neuro-fuzzy inference system (ANFIS) could be a technique that is suited for fatigue modelling. By integrating fuzzy logic into the neural network [32], it handles intermediate conditions which characterise relative truth, in contrary to the traditional Boolean logic where the outcomes are limited to 0 and 1 [33, 34]. This, as evaluated by Bowman et al. [35], is appropriate for fatigue assessment because of the uncertainties in fatigue studies. For example, scattering of high cycle fatigue data can be caused by the probabilistic nature of geometric factors such as defect and microstructure on crack initiation [36, 37]. In cases where the input and output variables are ill-defined, imprecise but meaningful representations of the system behaviour can be achieved using fuzzy logic. Besides, the ANFIS showed better error convergence for sparse data than the traditional neural network [38]. Such attributes are desirable for novel processes like the L-PBF, where fatigue data are not abundantly available and understanding of the underlying material science is still lacking. Successful applications of the ANFIS for fatigue modelling had been reported, such as in predicting the S-N properties of composite laminates [39, 40] and the fatigue threshold of a superalloy [38].

In this work, the ANFIS was examined for predicting the high cycle fatigue life of L-PBF stainless steel 316L samples, under the effects of varying processing/post-processing conditions and cyclic stresses. The dataset consists of 139 experimental fatigue data, part of which were used for training the model. Two models, using the processing/post-processing parameters and the tensile properties respectively as the inputs, were constructed. The model performance was evaluated by applying the models to the test data, as well as by cross validation with literature results.

2. Fatigue data

The dataset consists of 139 S-N data obtained from the authors' prior experimental works [27, 41-43]. Stainless steel 316L test blocks were fabricated on an EOS M290 L-PBF machine by varying the processing parameters, herein laser power P [27, 41], scan speed v [27] and layer thickness t [42], from the standard processing condition S_0, as shown in Figure 1. This resulted in parts with different defect characteristics, ranging from near fully dense parts with porosity fractions less than 0.1% to parts with porosity fractions close to 10%. Some of the S_0 samples were subjected to post-processing annealing or hot isostatic pressing (HIP) treatments [43], where annealing was done at two different

holding temperatures, i.e. 982 °C and 1093 °C, for 25 minutes each, and HIP was done at 1190 °C and 145 MPa for four hours. All samples were machined from the test blocks after fabrication, with the loading direction being perpendicular to the build direction (horizontal samples); this is with the exception of a set of samples that underwent HIP, for which the loading direction is parallel to the build direction (vertical samples). (Refer to the references for details of the experimental setup and samples dimensions.) Load-controlled fatigue tests were conducted under sinusoidal loading at a frequency of 5 Hz and load ratio of R = 0.1. Tensile properties were obtained by performing displacement-controlled tensile tests at a crosshead speed of 0.2 mm/min, using the same samples as the fatigue tests. In total, the variations in processing and post-processing strategies resulted in 18 sets of samples. The processing conditions and tensile test results, in terms of the ultimate tensile strength σ_b and elongation to failure δ, of the samples are summarised in Table 1.

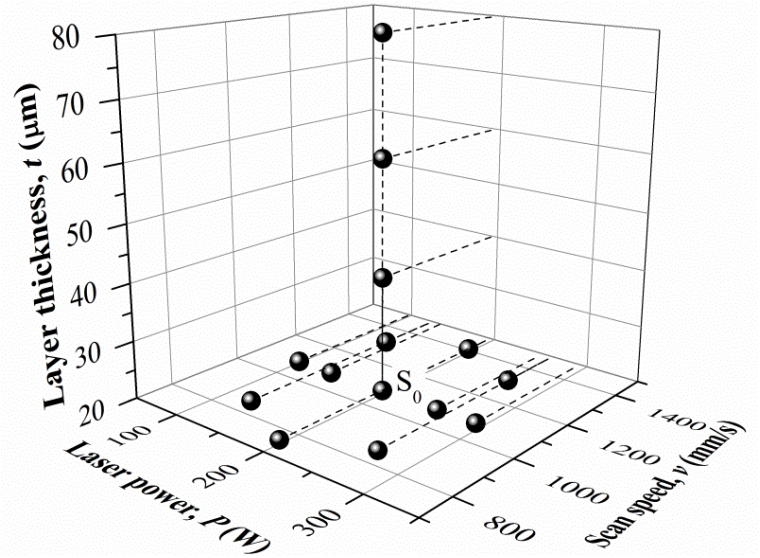

Figure 1 Laser powder bed fusion processing conditions used for fabricating the samples.

Table 1 Processing conditions, tensile properties and modes of high cycle fatigue failure of the dataset, collected from the authors' prior works [27, 41-43]. For tensile results, standard deviations are included where available. LOF stands for lack of fusion.

Sample	Processing/post-processing conditions				Tensile properties		Nature of crack
ID	P (W)	v (mm/s)	t (μm)	T	σ_b (MPa)	δ (%)	initiation/fracture
1/S_0	195	1083	20	As-built	723 ± 7	43 ± 2	Microstructure
2	293	1083	20	As-built	705	37	Microstructure/overheating defect
3	254	1083	20	As-built	725	38	Microstructure
4	137	1083	20	As-built	728	52	Microstructure/ single LOF defect

5	98	1083	20	As-built	631	28	Multiple LOF defects
6	195	758	20	As-built	708 ± 3	39 ± 5	Microstructure
7	195	1408	20	As-built	710 ± 2	45 ± 2	Microstructure
8	264	853	20	As-built	684 ± 3	30 ± 1	Microstructure
9	126	853	20	As-built	722 ± 2	46 ± 1	Microstructure
10	264	1313	20	As-built	712 ± 5	43 ± 2	Microstructure
11	126	1313	20	As-built	687 ± 6	38 ± 1	Single LOF defect
12	195	1083	40	As-built	717 ± 4	47 ± 1	Microstructure
13	195	1083	60	As-built	692	35	Single LOF defect
14	195	1083	80	As-built	507	17	Multiple LOF defects
15	195	1083	20	Annealed at 982 °C	673	52	Ratcheting
16	195	1083	20	Annealed at 1093 °C	665	56	Ratcheting
17	195	1083	20	HIPed (horizontal)	626 ± 3	54 ± 1	Ratcheting
18	195	1083	20	HIPed (vertical)	582 ± 8	67 ± 3	Ratcheting

3. Neuro-fuzzy modelling

3.1 Input variables

The fatigue failure modes of the samples are also listed in Table 1. Depending on the processing and post-processing conditions, three major types of failure behaviour were observed, i.e. 1) microstructure-driven crack initiation, 2) defect-driven crack initiation and 3) ratcheting-dominated deformation. Samples exhibiting the different failure mode constitutes about 55%, 21% and 24% of the dataset respectively. This section gives a brief description of the fracture behaviours for selecting the input variables of the model; refer to the references [27, 41, 43] for more in-depth discussions of the fracture behaviours and fractography analysis.

Microstructure-driven crack initiation concerns the near fully dense samples and is characterised by inter- and trans-granular fracturing. Competitive grain growth as a result of non-equilibrium solidification during L-PBF processing resulted in the formation of differently-oriented grain clusters [44, 45], as well as dislocation and second phase particles at the grain and sub-grain boundaries [46]. The attendant high local stress concentration at the grain boundaries promoted intergranular cracking

[47, 48], as shown in Figure 2a-b for Sample 4. Closely-packed ultrafine cellular sub-grains are clearly visible at the crack origin, indicating intergranular de-bonding. Within this processing region, cracking is very sensitive to microstructural heterogeneities, where the transition from intergranular- to transgranular-dominated fracture occurred at higher energy inputs, as shown in Figure 2c for Sample 3 and Figure 2d for Sample 8. The longer time for diffusion at slower cooling rate could have led to preferential clustering of second phase particles at the sub-grain boundaries rather than the grain boundaries, leading to the transgranular fracture [41]. Further increase in the energy input resulted in over-heating, where the evaporation of alloying elements caused degradation of the material properties [49, 50], as in the case of Sample 2. The lower resistance to cracking was found to trigger crack initiation from small porosities on the order of 10 μm [41].

With a reduction of the laser energy input, large irregular lack of fusion defects were formed because of poor layer-layer and track-track overlapping [51]. Intense stress fields at the sharp edges of the defects triggered defect-driven crack initiation, as shown in Figure 2e. With further reduction of the energy input, the defects increased both in size and number. Interaction among the closely-spaced defects led to enhanced stress fields, resulting in simultaneous crack initiation from multiple defects, as shown in Figure 2f. Samples associated with such failure modes are referred to as the porous samples in this work. Note that both microstructure-driven (Figure 2a) and defect-driven (Figure 2e) crack initiations were observed for Sample 4. As the size of the defects produced at this processing condition could be approaching the critical size that trigger the transition from microstructure-driven to defect-driven crack initiation, either failure mode could be possible depending on the microstructure and defect arrangements, e.g. size, orientation and location. This is an exemplification of the probabilistic nature of fatigue for L-PBF stainless steel 316L.

Ratcheting-dominated failure applies to the post-processed samples. The annealing or hot isostatic pressing procedure degraded the strength of L-PBF stainless steel 316L via recrystallization and grain growth [42]. As discussed in a prior work [43], the reduced tensile strength subjected the material to cyclic plastic deformation in the high cycle fatigue region, where the accumulation of plastic strains made ratcheting the relevant failure mechanism. The amount of ratcheting strain incurred is directly related to the extent of tensile strength reduction, i.e. the HIP samples are associated with the severest plastic deformation and lowest fatigue resistance, while the lower-temperature-annealed samples experienced the least plastic straining and reduction in fatigue resistance.

Figure 3 shows that samples exhibiting the different failure modes are associated with different trends in terms of the tensile strength and ductility properties. The near fully dense samples demonstrate the optimum tensile strength, in agreement with literature results [52]; the lower strength for Sample 8, as mentioned, is attributed to overheating. The elongations to failure for these samples show greater

variation, as ductility parameters are very sensitive to defects via the mechanism of strain-induced crack nucleation and growth [53]. The porous samples are characterised by concurrent reductions in strength and ductility with increasing defect fraction, consequent to the gross loss in load-bearing area and the increased propensity for cracking [52, 54]. For the post-processed parts, the increase in post-processing intensity is associated with lower strength but higher ductility, in compliance with the strength-ductility trade-off that is typical of structural metals [55].

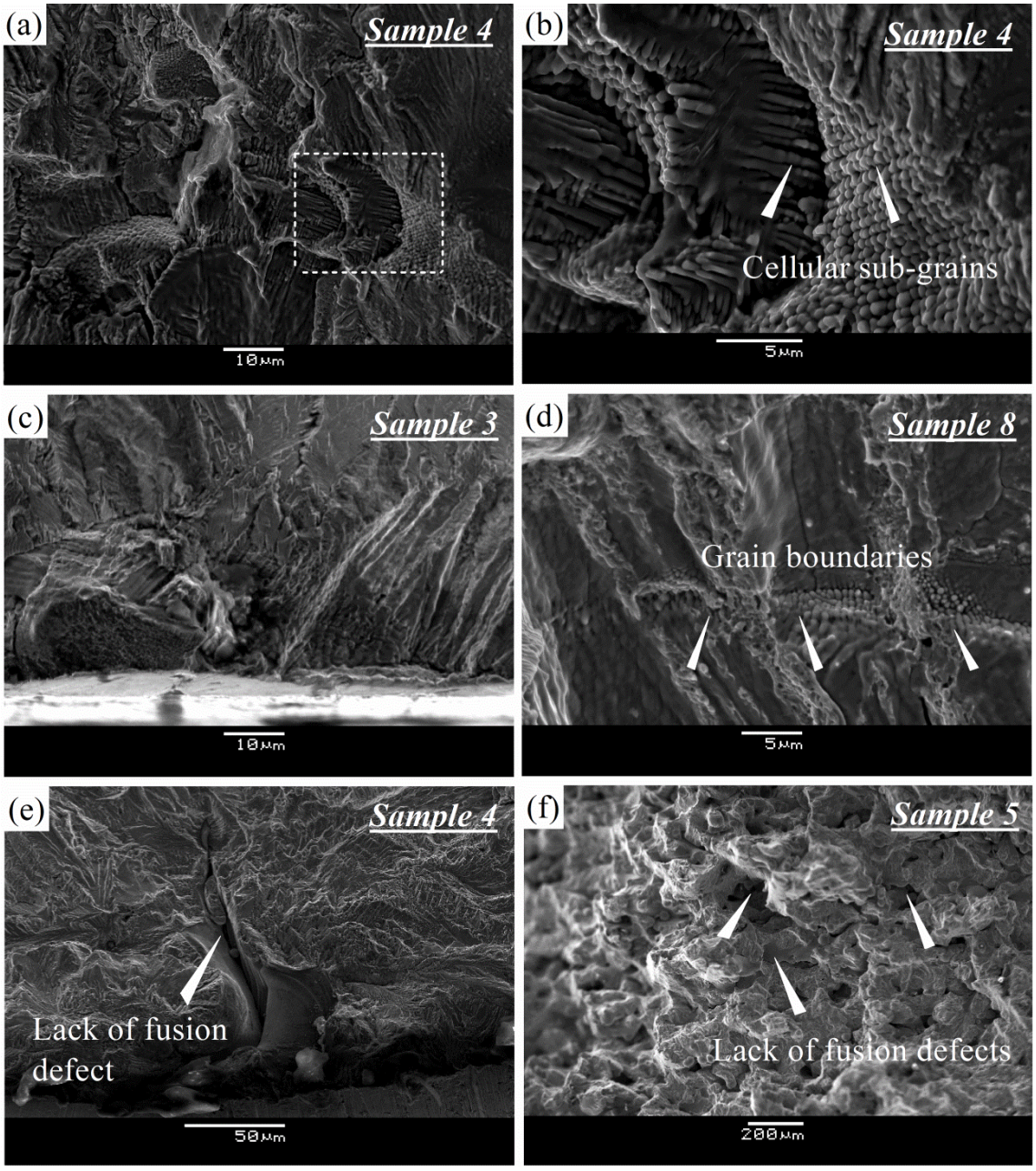

Figure 2 SEM fracture images showing crack initiation caused by (a) intergranular fracture, (b) enlarged view of highlighted region in (a); (c) and (d) transgranular fracture, (e) isolated lack of fusion defect and (f) multiple lack of fusion defects. Images are taken from the authors' earlier works [27, 41].

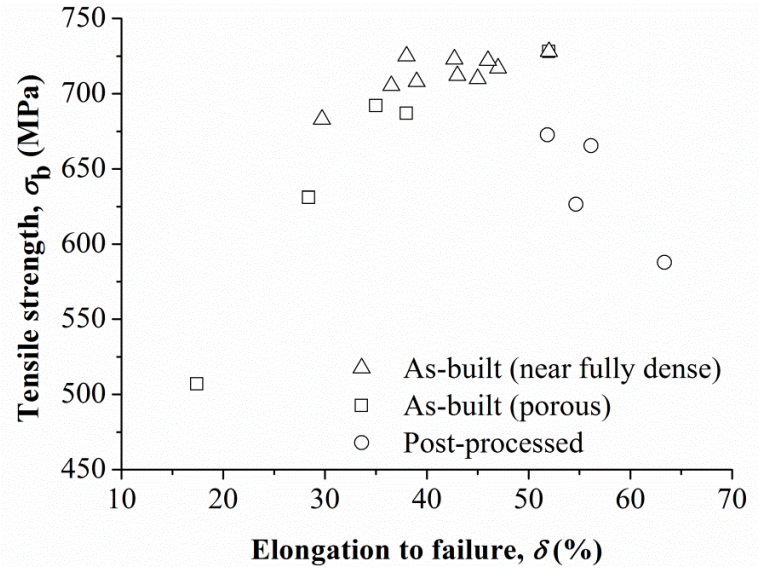

Figure 3 Ultimate tensile strength against elongation to failure of samples exhibiting different fatigue fracture behaviours. Data are taken from the authors' earlier works [27, 42, 43].

The above results indicate that the high cycle fatigue properties of L-PBF stainless steel 316L are related to the processing/post-processing strategies and the tensile properties. Therefore, two models, employing the different variables as the inputs, were implemented, i.e.

1) 'Process-based' model: the processing and post-processing parameters, i.e. P, v, t and T served as the inputs, where T was assigned with levels 1, 2, 3 and 4 for representing the as-built, low-temperature annealing, high-temperature annealing and HIP conditions respectively.
2) 'Property-based' model: the ultimate tensile strength σ_b and elongation to failure δ served as the inputs.

In addition, as the fatigue tests were conducted at a constant load ratio, the maximum applied cyclic stress σ_{max} was used for characterising the loading condition.

3.2 Architecture of the adaptive neuro-fuzzy inference system (ANFIS)

A typical feedforward neural network consists of three layers: an input layer, a set of hidden layers, and an output layer [56]. Each of the layers contains a number of nodes, known as neurons; signals are transmitted from the first layer to the last layer via the series of interconnected neurons. For neuro-fuzzy-based networks, the fuzzy inference system provides the rule base that forms the structure of the neural network, while the neural network algorithm manages the learning aspect by adapting model parameters according to the behaviour of the data [32]. In this work, 70% of the 139 data points was used for training the model, 15% for validation, where parameters of the trained models were fine-tuned by comparing the training and validation errors, while the remaining 15% was used

for testing the model performance. Figure 4 and Figure 5 show the architectures of the 'process-based' and 'property-based' ANFIS models respectively. As the 'property-based' model is associated with a simpler structure, it is used for explaining the ANFIS framework here.

The neural network structure of an ANFIS is formulated based on a set of 'if-then' rules, such as 'if x is A, then y is B' [57]. The *if* part of the rule is known as the antecedent or premise, and the *then* part is the consequent; the variables x and y are expressed in terms of A and B, which are linguistic labels that characterise concepts such as *very good*, *good*, *bad* and *very bad*. The 'property-based' model is made up of four rules, with the input parameters σ_b, δ and σ_{max} being partitioned into classes denoted by A_j, B_k, and C_l respectively. Neurons in Layer 1 are connected by arrows to neurons in Layer 2, forming the rules. For example, the first and second rules for the 'property-based' model in Figure 5 can be expressed respectively as:

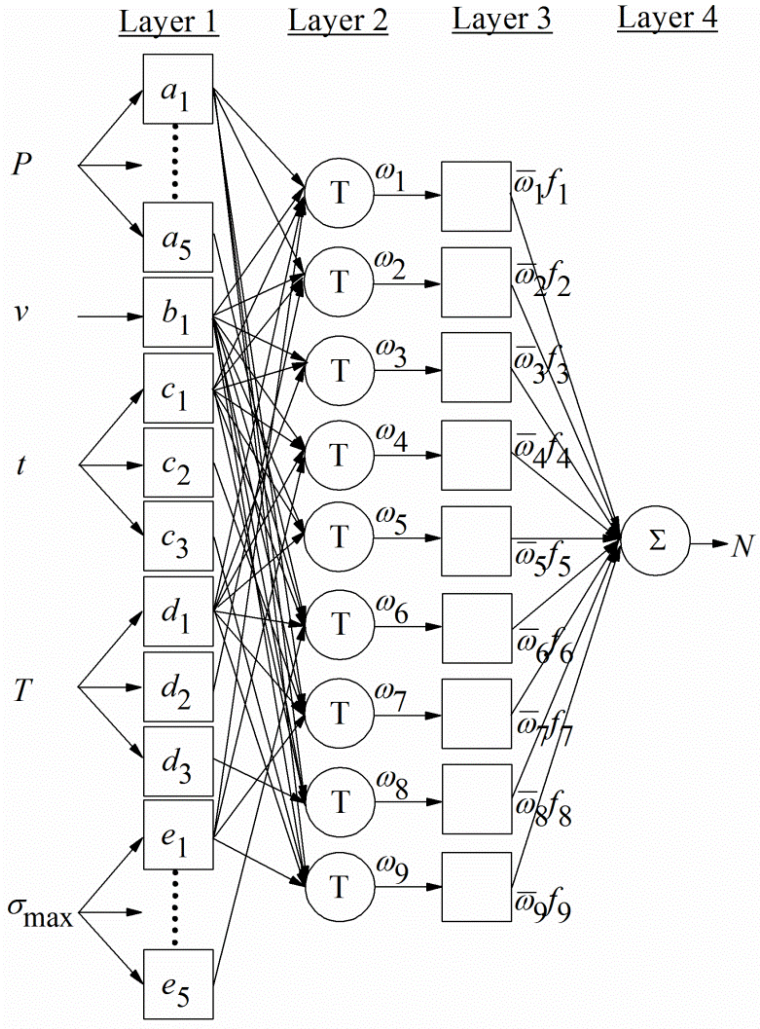

Figure 4 Structure of the adaptive neuro-fuzzy inference system (ANFIS) for the 'process-based' model.

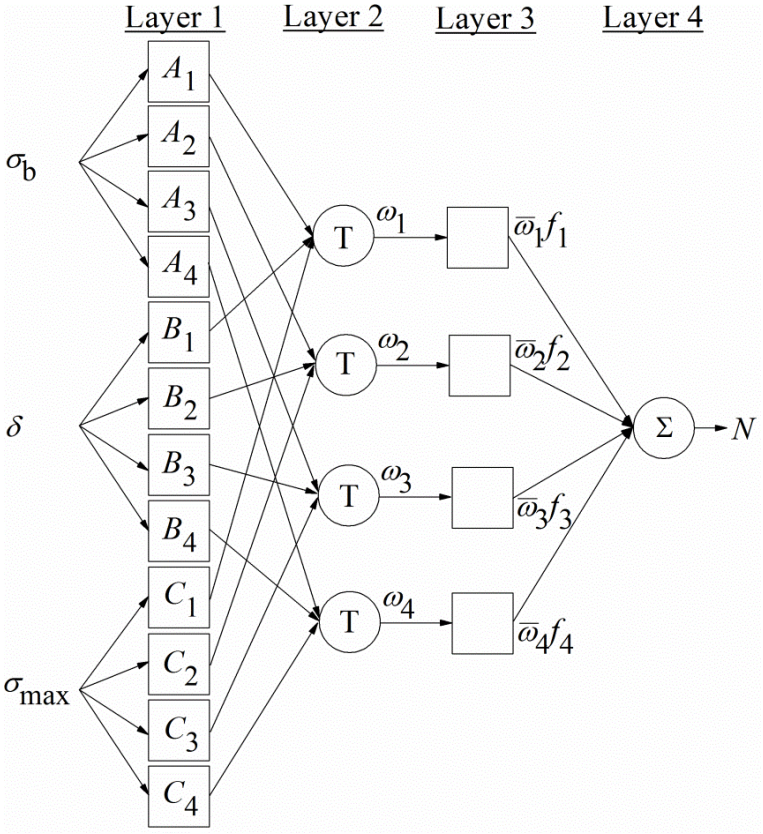

Figure 5 Structure of the adaptive neuro-fuzzy inference system for the 'property-based' model.

Rule 1: If σ_b is A_1, δ is B_1 and σ_{max} is C_1, then

$$f_1 = p_1\sigma_b + q_1\delta + r_1\sigma_{max} + s_1 \quad (1)$$

Rule 2: If σ_b is A_2, δ is B_2 and σ_{max} is C_2, then

$$f_2 = p_2\sigma_b + q_2 e + r_2\sigma_{max} + s_2 \quad (2)$$

where f_i is the linear consequent function of the ith fuzzy rule and p_i, q_i, r_i and s_i are the consequent parameters of the rule.

Steps of fuzzy reasoning include [32]: 1) deriving membership functions for the linguistic variables via fuzzification, 2) combining membership functions on the antecedent part of the rule using T-norm operators to produce the firing strength of each rule, 3) obtaining the consequents of the rules based on the firing strength, and 4) producing a crisp output by aggregating the consequents via the process of defuzzification. The nodal operations corresponding to each of the steps are described below:

Layer 1: Nodes in the first layer specify the degrees to which the given inputs belong to each of the linguistic labels in terms of the membership functions μ:

$$O_j^1 = \mu_{Aj}(\sigma_b),\ j = 1, 2, 3, 4 \quad (3)$$

$$O_k^1 = \mu_{Bk}(\delta),\ k = 1, 2, 3, 4 \quad (4)$$

$$O_l^1 = \mu_{Cl}(\sigma_{max}),\ l = 1, 2, 3, 4 \quad (5)$$

Membership functions can adopt the forms of the triangular, trapezoidal, Gaussian or bell-shaped functions [58]. The latter two are often used for representing fuzzy sets because of the smooth distribution curves [59]. In this work, the Gaussian distribution was used as it contains one parameter less than the bell-shaped distribution. Good modelling accuracy had been reported for ANFIS models that utilised this membership function for fatigue life prediction [39, 40]. For example, the membership function μ_{Aj} for the variable σ_{b} is expressed as:

$$\mu_{Aj}(\sigma_b) = \exp\left[\frac{-(\sigma_b - \alpha_j)^2}{2\beta_j^2}\right],\ j = 1, 2, 3, 4 \quad (6)$$

where α_{j} and β_{j} are parameters of the Gaussian distribution.

Layer 2: Nodes in this layer perform the T-norm operation, where membership values corresponding to each fuzzy rule are multiplied:

$$O_i^2 = \ \omega_i = \mu_{Aj}(\sigma_b) \times \mu_{Bk}(\delta) \times \mu_{Cl}(\sigma_{max}),\ i = 1, 2, 3, 4 \quad (7)$$

The output ω_{i} is the firing strength, also known as the 'degree of fulfilment', of a particular rule. As the ANFIS model contains four fuzzy rules, *i* goes up to a value of four.

Layer 3: Output of a node in this layer is equal to the product of the normalized firing strength, i.e. the ratio of the *i*th rule's firing strength to the summation of the firing strengths of all the rules, and the consequent function f_{i} of the rule:

$$O_i^3 = \bar{\omega}_i f_i \quad (8)$$

Layer 4: This layer constitutes the summation of all incoming signals, from which the fatigue life *N* is predicted:

$$O_1^4 = \log(N) = \sum_i \bar{\omega}_i f_i \quad (9)$$

Note that the logarithmic values of *N* were used for modelling to avoid extreme differences in fatigue lives, which are within the range of $10^3 - 10^6$ cycles for the dataset. The square nodes, i.e. Layer 1 and Layer 3, are adaptive nodes where the parameters are optimized by the adaptive neural network. For supervised learning, models learn by direct comparison of the predicted outputs with the actual values

in order to minimise the error function, in this case, the root mean squared (RMS) error. Gradient descent-based method can be used for tuning the parameters of the ANFIS [60], but because of its tendency to be trapped in local minima, the hybrid learning rule, which combines the gradient method and least square estimation, is often preferred [61] and is used in this work. All computations and model developments were performed using the Neuro-Fuzzy Designer app in Matlab.

3.3 Extraction of fuzzy rules by data clustering

For large multivariate datasets, clustering is often performed to identify natural groupings in the data so as to allow a concise representation of the system behaviour. For ANFIS, clustering is used as a rule extraction algorithm where the cluster centres provide the basic premises of the rule base [62, 63]. Specifically, it partitions the input variables into classes, as demonstrated by the neurons in Layer 1 of the ANFIS model; neurons belonging to the same cluster centre are connected in Layer 2, leading to the respective rules. This technique serves to initialise the ANFIS structure, where the model parameters are subsequently tuned by the neural network during training to fit the data. Values of α for the Gaussian membership functions characterise the cluster centres after parameter tuning.

Subtractive clustering was performed on the training datasets using the Clustering tool in Matlab. The algorithm carried out the following steps for extracting the cluster centres [64, 65]: 1) the point with the highest potential, based on calculation of the Euclidian distances with respect to all other data points, was chosen as the first cluster centre; 2) data points in the neighbouring regions of the first cluster centre, based on a predefined range of influence (ROI), were deleted and the remaining point with the highest potential was selected as the next cluster centre; 3) these steps were repeated until all data points are in the range of a cluster centre. The ROI, a scalar quantity that adopts value between [0, 1], is a key parameter in subtractive clustering as it affects the range of the data points around a cluster centre that are removed: a larger ROI yields bigger and less cluster centres [65], and vice versa.

As the ROI is directly related to the number of fuzzy rules, suitable ROI value can be determined by evaluating the performance of the corresponding ANFIS model. Prediction error generally decreases with increase in model complexity as the larger number of model parameter allows more explicit representation of the system behaviour [66]. However, overfitting occurs when the increase in model complexity does not only lead to better fitting of the trends in the data, but also the noises. This impinges on the model performance when applying the model to a fresh set of data, in this case, the validation set. Figure 6 shows the training and validation errors as a function of the number of fuzzy rules, obtained by varying the ROI. For both the ‘process-based’ and ‘property-based’ models, the training errors decrease with the number of fuzzy rules, as expected. The validation errors, however, increase following the initial reductions. This is suggestive of overfitting as the model is unable to

generalise to the unseen data despite the increase in model complexity. Therefore, to prevent overfitting, the numbers of fuzzy rules were selected for the conditions with the smallest validation errors before they start diverging. This led to nine rules for the 'process-based' model (ROI = 0.65) and four rules for the 'property-based' model (ROI = 0.5), as highlighted in Figure 6.

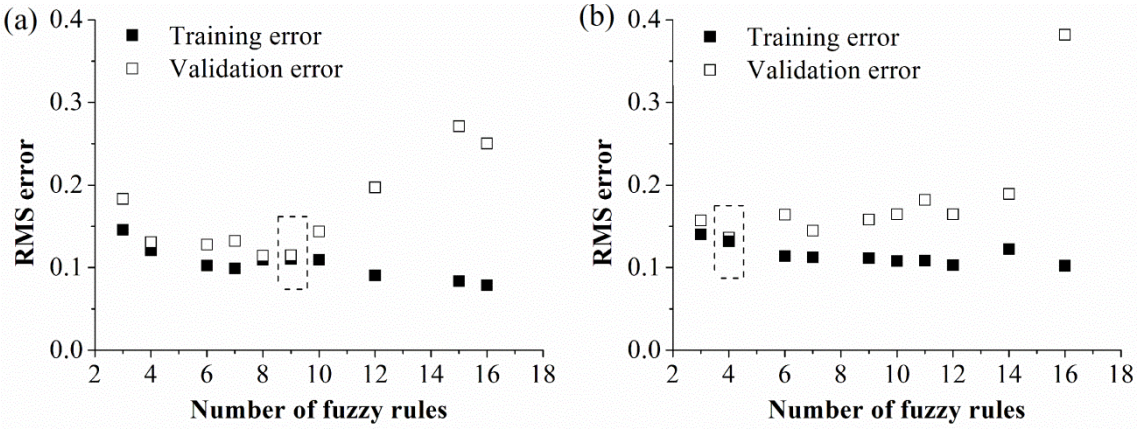

Figure 6 Training and validation errors as a function of the number of fuzzy rules for the (a) 'process-based' model and (b) 'property-based' model. Selected conditions for model construction are highlighted.

4. Results and discussion

This section examines the validity of the computationally-derived fuzzy inference system vis-à-vis the fracture behaviours of the samples. The accuracy of life prediction is demonstrated for the training and test datasets, while the generalisation capability of the models is evaluated by applying them to literature data.

4.1 Fuzzy representation of the fracture modes

For the 'process-based' model, the input variables P, v, t, T and σ_{max} were partitioned into a set of 5-1-3-3-5 Gaussian-type membership functions, which are schematically shown in Figure 7. By carefully examining the membership functions constituting the antecedents of the fuzzy rules, five out of the nine rules were found to characterise the effects of P and v at $t \approx 20$ μm and $T \approx 1$, two rules for the effects of t, with P and v at the standard processing conditions and $T \approx 1$, and two rules for the effects of T, with P, v, and t at the standard processing conditions. This is in agreement with the distribution of the input data shown in Figure 1, indicating that the rules were derived according to the different sample classes.

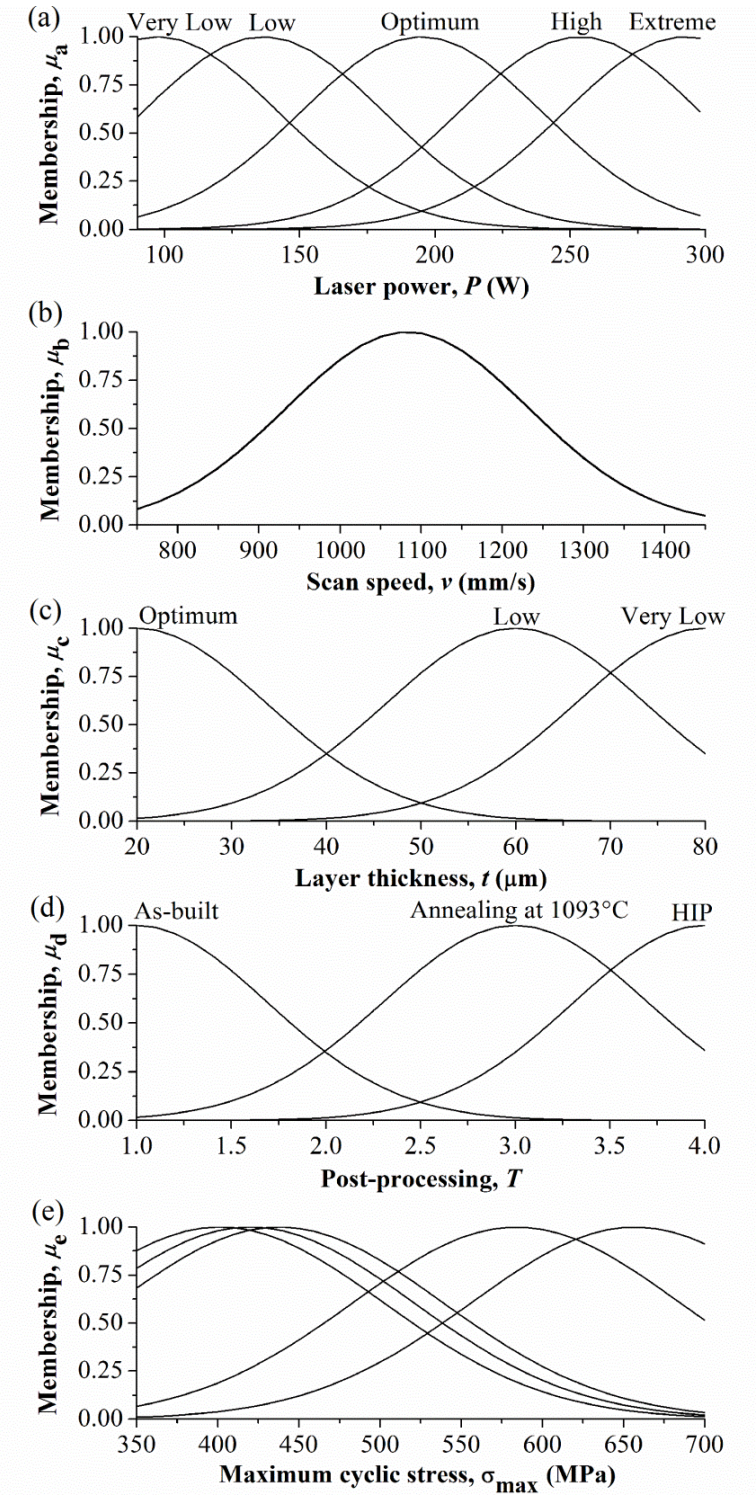

Figure 7 Membership functions for the 'process-based' model: (a) laser power, (b) scan speed, (c) layer thickness, (d) post-processing intensity and (e) maximum cyclic stress.

Figure 8 shows the fatigue life contour plot, taken from a prior work [27], as a function of P and v for the as-built samples fabricated at t = 20 μm (Samples 1-11) and fatigue tested at σ_{max} = 657 MPa. Values of α of the membership functions for the five rules characterising the effects of P and v are indicated by the black dots. They are conveniently referred to as the 'cluster centres' in this work,

though it is to be noted that their values differ slightly from the initial cluster centres obtained from subtractive clustering due to parameter tuning by hybrid learning, as mentioned in Section 3.3. It can be seen that the locations of the 'cluster centres' correspond to some of the major fatigue life regions. In fact, they coincide with the processing conditions of Samples 1-5, which are samples that exemplify the different fracture modes of the as-built parts, as specified in Table 1. Based on this observation, linguistic labels such as *Very Low*, *Low*, *Optimum*, *High* and *Extreme* can be assigned to the membership functions for *P* (Figure 7a). Specifically, the *Optimum* level ($P \approx 195$ W) refers to processing conditions that produce the optimum fatigue properties; the *Low* ($P \approx 137$ W) and *Very Low* ($P \approx 98$ W) levels pertain to crack initiation from single and multiple defects respectively, while the *High* ($P \approx 254$ W) and *Extreme* ($P \approx 293$ W) levels are associated with the transition to transgranular-dominated crack initiation and the generation of critical over-heating-induced defects respectively. Note that the use of membership functions, in contrast to the Boolean logic, for describing the input variables is appropriate, as the change from one fracture mode to another is not triggered by abrupt changes in the input settings, but by a gradual transition.

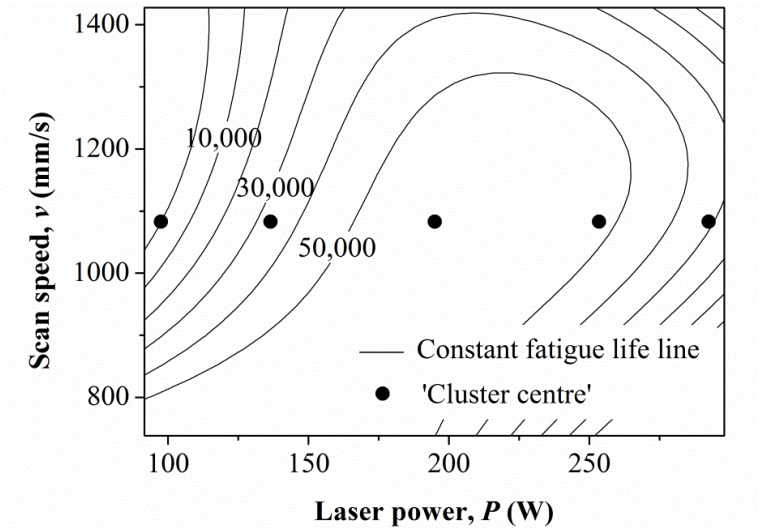

Figure 8 Locations of the 'cluster centres' for the 'process-based' model on the fatigue life contour plot as a function of laser power and scan speed for as-built samples fabricated at layer thickness of 20 μm and fatigue tested at σ_{max} = 657 MPa, adapted from a prior work [27].

Similar analysis applies to the membership functions for layer thickness (Figure 7c), where the primary fatigue cracks originate from a single defect at $t \approx 60$ μm (*Low* level), and from multiple defects at $t \approx 80$ μm (*Very Low* level). They contributed to the two rules that characterise the effects of *t*. For the post-processing variable *T*, membership functions were identified for the as-built, high-temperature annealing and hot isostatic pressing conditions (Figure 7d), where the increase in post-processing intensity correlates directly with the extent of fatigue strength degradation due to cyclic plastic deformation, as explained in Section 3.1. This is responsible for the two rules corresponding to

the effects of *T*. Membership functions for σ_{max} (Figure 7e) are dependent on the actual stresses applied for the fatigue tests and did not contribute to any additional fuzzy rules.

A simpler ANFIS structure with 4-4-4 membership sets was obtained for the 'property-based' model, as illustrated in Figure 9. Figure 10 shows the 'cluster centres' in relation to the tensile properties of the dataset. The σ_b-δ pairs forming the premises of Rules 1 and 2 correspond to the tensile properties of the near fully dense samples, while those for Rules 3 and 4 correspond to the post-processed and porous samples respectively. Note that rules were generated for two different cyclic stresses for the near fully dense samples but not for the other sample types. This could be attributed to the larger percentage of input data belonging to this group (55% of the dataset). As the clustering algorithm defines cluster centre by calculating the potential of a data point in terms of its distance to all other data points, high density region with many neighbouring data, such as the near fully dense samples, are more likely to be chosen as the cluster centre [64].

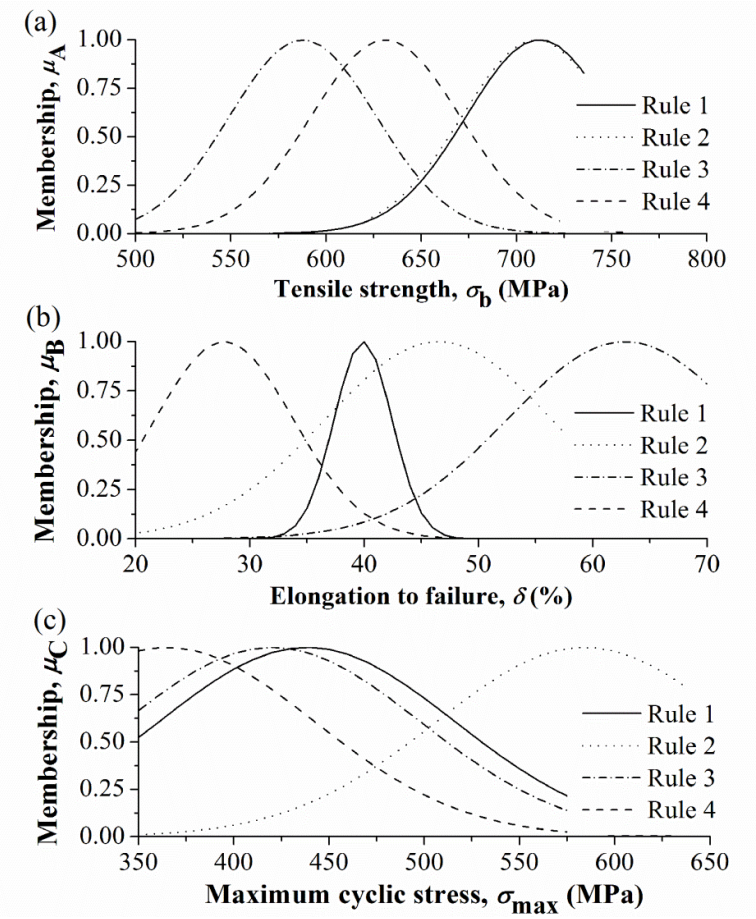

Figure 9 Membership functions for the 'property-based' model: (a) tensile strength, (b) elongation to failure and (c) maximum cyclic stress.

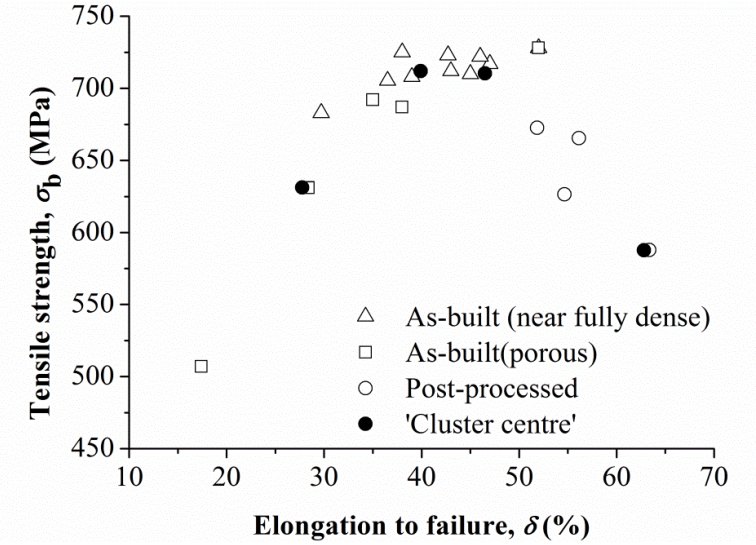

Figure 10 Locations of the 'cluster centres' for the 'property-based' model in relation to the tensile strength and elongation to failure of the samples.

In summary, the above results indicate that regardless of the input variables, subtractive clustering effectively captured the underlying fracture mechanisms of the dataset. The assignment of fuzzy rules based on the cluster centres ensured mapping of the input-output relationships in accordance to the fracture behaviours of the samples.

4.2 Life prediction

Table 2 lists the RMS errors obtained from applying the models. The overall RMS errors range from about 11% to 16% across the datasets. In a similar study by Vassilopoulos et al. [39], where the ANFIS was used for predicting the high cycle fatigue life of composite laminates, the training and test errors were reported to be 25% and 47% respectively (for a model constructed using the same percentage allocation of training data as this work). The better prediction accuracy achieved in this work could be attributed to the simpler system behaviour of the dataset (consider that a 15-17-rule model was obtained by Vassilopoulos et al. for a dataset of 257 experimental data). An increase in the complexity of the data, e.g. one that involves a larger number of input variables and bigger processing region, is likely to impinge on the modelling performance. This is discussed further in the context of applying the model to literature data in Section 4.3.

The RMS errors for the individual sample types expand a bigger range, from about 9% to 21%. Worth noting is that the porous samples are associated with the greatest errors which consistently surpass the overall errors, while errors for the near fully dense samples tend to be the least and are always less than the overall errors. The good prediction accuracy for the near fully dense condition stems from the large amount of data belonging to this sample group. The more representative dataset ensured more

effective training, as evidenced in the larger number of cluster centres/rules corresponding to the input space of these samples. Between the porous and post-processed conditions, which have similar data distributions, the worse modelling performance of the former could be caused by a few reasons. For the 'process-based' approach, fabrication of the porous samples incurred the processing variables P, v and t, while post-processing is a function of T only. The synergistic effects of the input variables for the porous samples could have resulted in greater variance, thereby the larger prediction errors. For the 'property-based' model, note that the tensile properties of some of the porous samples, i.e. Samples 11 and 13 (crack initiation from single defect), are very close to those of the near fully dense samples (e.g. Samples 2 and 6). Despite the different fatigue properties between the two types of samples, the similar input values will lead to similar model predictions. Figure 11 compares the error distributions for the samples. It can be seen that the histogram for the porous samples shows a heavy right tail, which is indicative of overestimations, while the opposite trend applies for the near fully dense samples. This is reasonable because as the model sought to minimise the sum of squared errors according to the least squares method, it arrived at solutions that approximate the average fatigue lives of the two types of samples. The resulting biased predictions, however, are not desirable, especially for the porous samples as they can lead to unconservative estimates of the fatigue properties.

Table 2 Root mean squared errors obtained from applying the 'process-based' and 'property-based models.

Model/data type		RMS errors (%)			
		As-built (near fully dense)	As-built (porous)	Post-processed	Overall
'Process-based'	Training data	8.84	14.82	10.80	10.86
	Test data	13.76	20.87	15.24	16.00
'Property-based'	Training data	11.32	16.44	13.61	13.09
	Test data	14.55	18.58	11.93	14.66

Figure 12 compares the predicted and experimental fatigue lives. The predicted results are generally within a factor of two of the experimental data, even for the porous samples which are associated with the greatest errors. Figure 13 presents the results for selected samples on S-N plots. With the exception of Sample 6 (Figure 13b) and Sample 13 (Figure 13d), the predicted S-N curves fit well the experimental data across the different failure modes. It is worth noting that the predicted result at each loading condition is generally within the experimental scatter band, indicating that the models are able to account for variations in the dataset due to fatigue scatter. For Samples 6 and 13, the biased predictions from applying the 'property-based' model are evident, with the overestimation for Sample

13 amounting to a factor of about 1.7 on life. Nonetheless, the results are acceptable considering the extent of variation in fatigue data due to scatter.

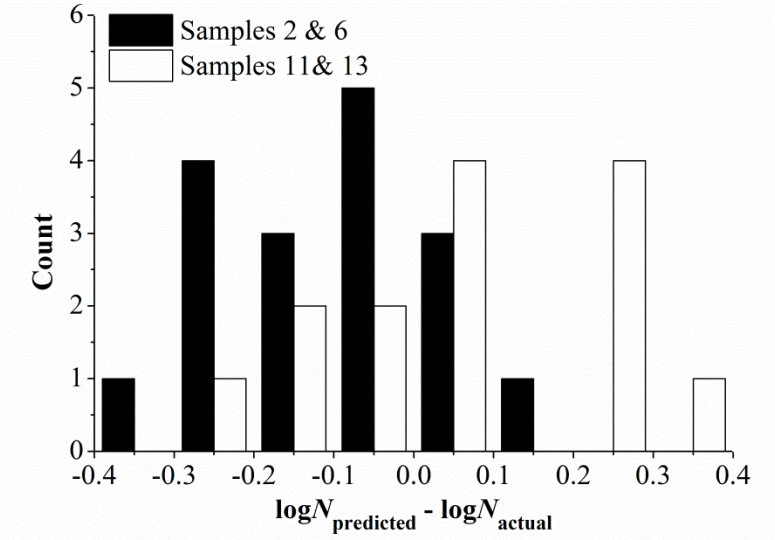

Figure 11 Histograms showing the error distributions for Samples 11 and 13 and Samples 2 and 6 for the 'property-based' model.

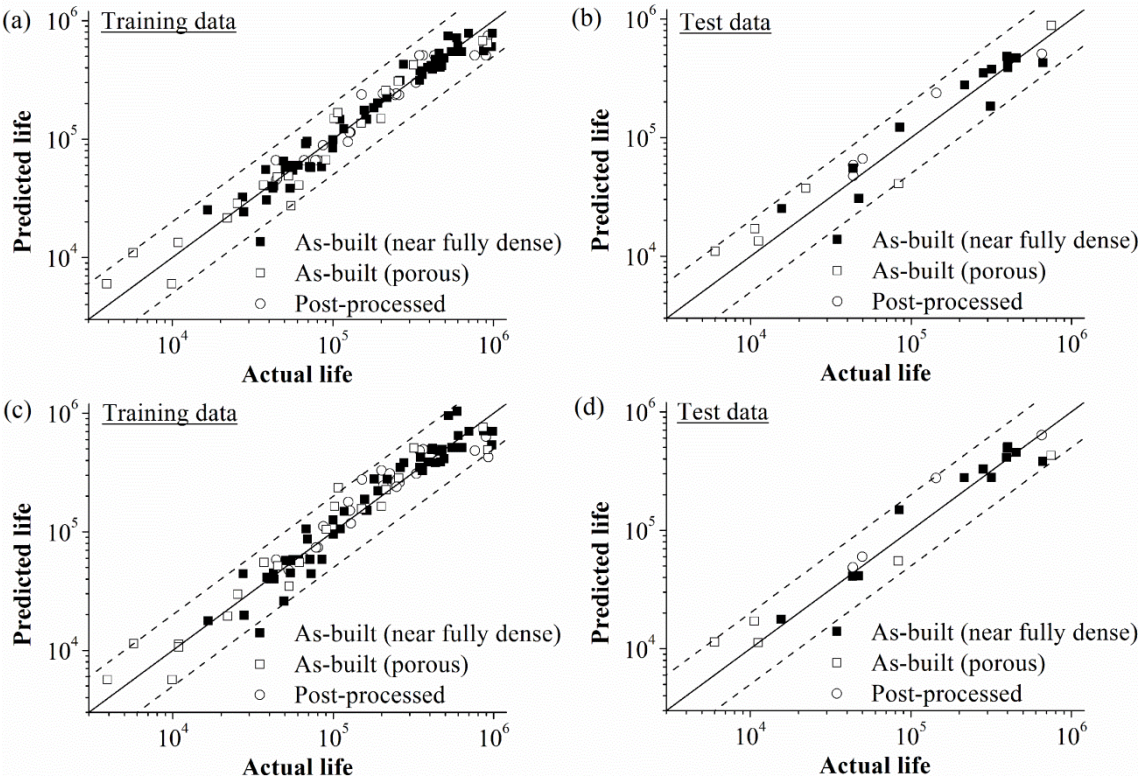

Figure 12 Actual and predicted fatigue lives (load cycles) for the (a) training and (b) test data of the 'process-based' model, and for the (c) training and (d) test data of the 'property-based' model. Dotted lines represent factor of two on life.

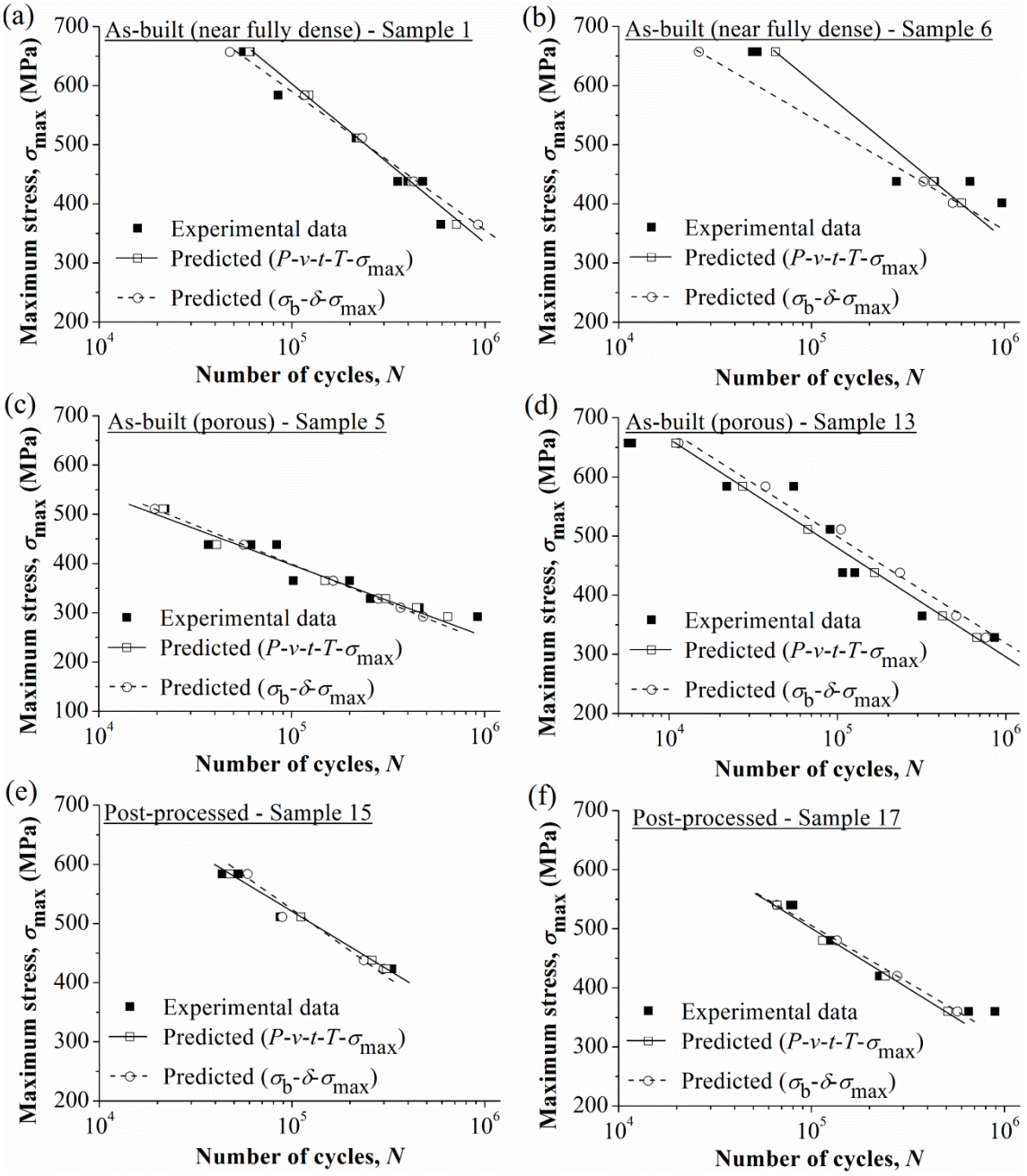

Figure 13 Comparison of experimental and predicted S-N data for (a)-(b) near fully dense samples, (c)-(d) porous samples and (e)-(f) post-processed samples.

In relation to the underlying working mechanism of the ANFIS, the good prediction capability, despite the diverse mix of fatigue properties and fracture behaviours of the dataset, can be attributed to the decomposition of the modelling task by the fuzzy rules [40]. For a given set of inputs, only rules corresponding to the specific input class are activated for life prediction. By dividing the design space into the sub-regions/clusters, with each being managed by the respective fuzzy rule, the dimensionality of the system is significantly reduced, leading to the good modelling performance.

4.3 Application of the model to literature data

The generalisation capability of the ANFIS for high cycle fatigue life prediction was demonstrated using literature data [67-69]. Details of the sample and fatigue test conditions are listed in Table 3. Only the 'property-based' model was examined as complete input information for the 'process-based' model was not always available. Data pre-processing was done to adjust for the effects of fatigue loading: the Walker equation, based on a Walker parameter of 0.527 [70], was applied to the results of Leuders et al. [68] and Mower and Long [69] to account for the load ratio effect; a modifying factor of 0.85 on fatigue strength was applied to the results of Mower and Long to adjust for the bending load [71].

Table 3 Fatigue test and sample conditions (build orientation and post-processing treatment), number of S-N data, and tensile properties of literature data used for validating the 'property-based' model.

References	Fatigue test condition	Sample condition	Number of S-N data	Tensile properties	
				σ_b (MPa)	δ (%)
Spierings et al. [67]	Axial, R = 0.1	#1 Vertical as-built, machined	12	760	30
		#2 Vertical as-built, polished	14	760	30
Leuders et al. [68]	Axial, R = -1	#1 Vertical as-built, machined	8	600	55
		#2 Vertical, machined, heat treated at 650 °C	8	618	54
		#3 Machined, HIPed	3	587	64
Mower and Long [69]	Bending, R = -1	#1 Horizontal, stress relieved	11	717	28
		#2 45° inclined, stress relieved	10	680	30

Results from applying the 'property-based' model to the literature data are shown in Figure 14. A range of prediction accuracies was obtained depending on the dataset. Specifically, the model produced reasonable results for the heat treated samples of Leuders et al., but not for the other samples by the same authors, especially at the lower and higher fatigue life regions. Results for Spierings et al. and Mower and Long were significantly overestimated, by as much as over an order of magnitude in the extreme cases. Mismatched material properties reported by the studies were likely to have contributed to the varied modelling performance. For example, the tensile strengths of 760 MPa and 717 MPa, reported by Spierings et al. and Mower and Long respectively, are higher than those for samples with equivalent ductility values used in this work. As the higher tensile strength implies better fatigue resistance, the fatigue lives were overestimated. For the HIP samples used by Leuders et al., as the tensile properties are comparable with this work, the poor predictions are suggestive of

dissimilar fatigue properties. Noteworthy also is the considerably worse predictions for the inclined samples than the horizontal samples of Mower and Long despite the similar tensile properties. This is a result of actual difference in the experimentally determined S-N data, which, as noted by the authors, could have been caused by surface defects that promoted premature failure of the inclined samples.

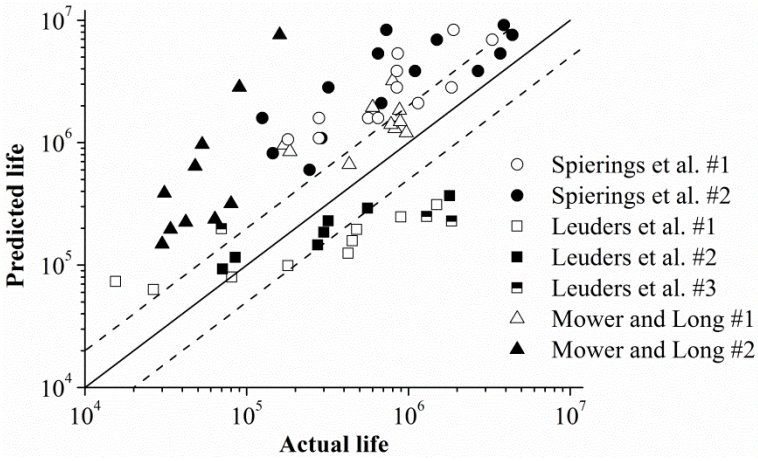

Figure 14 Actual and predicted fatigue lives (load cycles) obtained from applying the 'property-based' model to literature data. Dotted lines represent factor of two on life.

The mismatched material properties exemplify the machine-to-machine and the associated processing variabilities of L-PBF parts [18, 27, 72]. This limits the transferability of models constructed based on a set of experimental results to parts made by other L-PBF systems and processing conditions. Different fatigue test setup could also have contributed to the poor prediction accuracy. To improve modelling performance, the system behaviour of the new experimental space needs to be taken into account. This can be achieved by: 1) selection of input variables that characterise the behaviour of the new design space; 2) incorporating the literature data into the dataset for training the model.

A systematic approach to input parameter selection can be achieved using statistical methods. For example, by conducting design of experiments with 1000 design points, Bessa et al. [73] identified variables, including microstructure, material property and external condition, as the relevant inputs for toughness modelling. While the 'process-based' or 'property-based' variables demonstrated good correlations with the fatigue properties for the present dataset, for complex high dimensional data, a combination of the variables may be necessary for complete descriptions of the input-output space. Microstructure-based inputs, e.g. defect and grain sizes, texture, that are associated with more fundamental representations of the crack driving force and cyclic plastic deformation, may lead to improved correlation with the crack initiation properties [74]. Moreover, considering the machine-to-machine variability, the machine model may be a key metric for describing the fatigue properties of L-PBF parts.

Expanding the database by incorporating the literature data serves to provide the needed information for learning, which is the basis of 'big data' analytics [75]. By combining the reference data with the data in this work, a new dataset with 205 data points was constructed. Following the same procedures outlined in Section 3, and including the load ratio as an additional input parameter, a 6-rule ANFIS model was obtained. This led to marked improvements in the prediction accuracy across the different sources of data, as shown in Figure 15. The overall RMS errors are larger than those for the original model, at 17.41% for the training data and 20.25% for the testing data, because of the increased data complexity. Nonetheless, the errors are acceptable considering the fatigue scatter, which is evaluated at a factor of two on life.

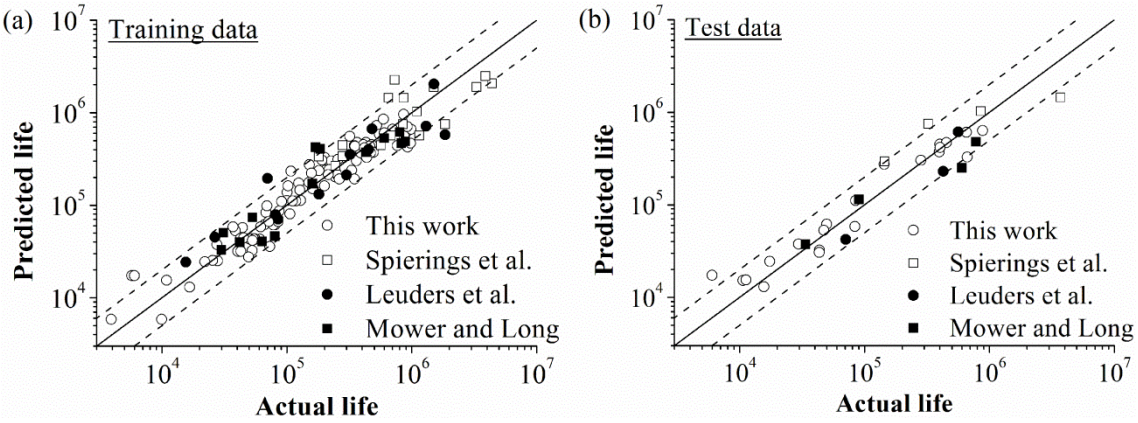

Figure 15 Actual and predicted fatigue lives (load cycles) for the (a) training and (b) test data of ANFIS model constructed using literature data and data from this work.

The better modelling performance can be appreciated by examining the fuzzy rules. Figure 16 shows the locations of the 'cluster centres' on the σ_b-δ plot. In comparison with the original 'cluster centres' in Figure 10, three new 'cluster centres' were extracted. The locations of the cluster centres correspond to the tensile properties of the literature data, indicating that the clustering algorithm correctly captured the oddities in the data and assigned new rules for prediction. Task decomposition by the rule-based approach reduced the dimensionality of the problem, such that the use of the tensile properties as the inputs is still valid. Worth noting also is the small amount of data needed for training the model (e.g. 13 data points only for Leuders et al.). The strong versatility and adaptability of the ANFIS suggest the possibility of extending the model to highly complex systems, e.g. one that involves more processing variables, machine models and material types, provided sufficient training data are available.

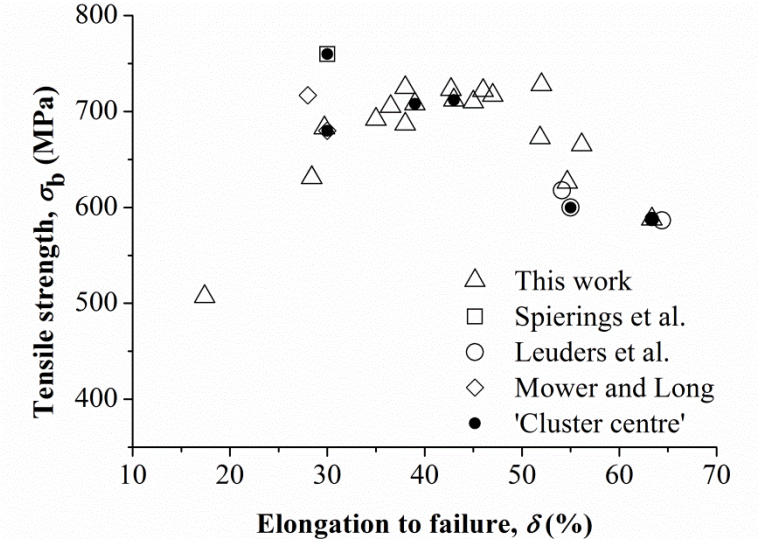

Figure 16 Locations of the 'cluster centres' for the ANFIS model constructed by incorporating the literature data into the dataset, in relation to the tensile strength and elongation to failure of the samples.

5. Conclusions

This study examined the adaptive neuro-fuzzy-based machine leaning technique for modelling the high cycle fatigue life of L-PBF stainless steel 316L. The following conclusions could be drawn from the results obtained:

1) The ANFIS method successfully predicted the fatigue life of L-PBF stainless steel 316L samples showing a wide range of material properties and fracture behaviours, arising from the use of different processing/post-processing conditions, and subjected to different cyclic stress levels. The models effectively captured the characteristic failure modes of the dataset, which formed the rule base for fatigue life predictions.
2) Both the processing/post-processing parameters and tensile properties can be used as the inputs for constructing the ANFIS, as demonstrated by the 'process-based' and 'property-based approaches. For real life engineering practices, these approaches can be adopted concurrently, for quality assurance at the manufacturing stage and property assessment stage respectively.
3) The transparency offered by the linguistic rules allowed better appreciation of the model, aided the selection of model parameters and simplified the model design and validation process. This is an advantage of the ANFIS over the non-fuzzy-based learning approaches. Besides, the use of fuzzy boundaries could have allowed better tolerance for imprecise data, such that the models could effectively account for the presence of scatter in the S-N data.
4) Results from applying the model to literature data indicate that the applicability is restricted to the experimental space over which it is trained. The selection of representative input variables and

construction of a large database for training are important for improving the generalisation capability of the model.

Acknowledgement

This work was supported by the Singapore Economic Development Board (EDB) Industrial Postgraduate Programme (IPP).

References

[1] I. Gibson, D.W. Rosen, B. Stucker, Additive manufacturing technologies, Springer2014.

[2] D. Bak, Rapid prototyping or rapid production? 3D printing processes move industry towards the latter, Assembly Automation 23(4) (2003) 340-345.

[3] N. Hopkinson, P. Dickens, Rapid prototyping for direct manufacture, Rapid prototyping journal 7(4) (2001) 197-202.

[4] M.J. Galba, M. Reischle, Additive manufacturing of metals using powder-based technology, Additive Manufacturing, CRC Press (2015) 97-142.

[5] H. Bikas, P. Stavropoulos, G. Chryssolouris, Additive manufacturing methods and modelling approaches: a critical review, Int. J. Adv. Manuf. Technol. 83(1) (2016) 389-405.

[6] C. Yap, C. Chua, Z. Dong, Z. Liu, D. Zhang, L. Loh, S. Sing, Review of selective laser melting: Materials and applications, Appl. Phys. Rev. 2(4) (2015) 041101.

[7] M. Yakout, A. Cadamuro, M. Elbestawi, S.C. Veldhuis, The selection of process parameters in additive manufacturing for aerospace alloys, 92 (2017) 2081-2098.

[8] Y. Li, D. Gu, Parametric analysis of thermal behavior during selective laser melting additive manufacturing of aluminum alloy powder, Mater. Des. 63 (2014) 856-867.

[9] L. Thijs, F. Verhaeghe, T. Craeghs, J.V. Humbeeck, J.-P. Kruth, A study of the microstructural evolution during selective laser melting of Ti–6Al–4V, Acta Mater. 58(9) (2010) 3303-3312.

[10] Y. Murakami, Metal fatigue: effects of small defects and nonmetallic inclusions, 1st ed. ed., Elsevier, UK, 2002.

[11] P. Li, D. Warner, A. Fatemi, N. Phan, Critical assessment of the fatigue performance of additively manufactured Ti–6Al–4V and perspective for future research, Int. J. Fatigue 85 (2016) 130-143.

[12] A. Yadollahi, N. Shamsaei, S.M. Thompson, A. Elwany, L. Bian, Effects of building orientation and heat treatment on fatigue behavior of selective laser melted 17-4 PH stainless steel, Int. J. Fatigue 94 (2017) 218-235.

[13] E. Wycisk, A. Solbach, S. Siddique, D. Herzog, F. Walther, C. Emmelmann, Effects of defects in laser additive manufactured Ti-6Al-4V on fatigue properties, Physics Procedia 56 (2014) 371-378.

[14] S. Tammas-Williams, P. Withers, I. Todd, P. Prangnell, The influence of porosity on fatigue crack initiation in additively manufactured titanium components, Scientific Reports 7 (2017).
[15] H.R. Ammar, A.M. Samuel, F.H. Samuel, Effect of casting imperfections on the fatigue life of 319-F and A356-T6 Al–Si casting alloys, Mater. Sci. Eng. A 473(1) (2008) 65-75.
[16] L. Liu, Q. Ding, Y. Zhong, J. Zou, J. Wu, Y.-L. Chiu, J. Li, Z. Zhang, Q. Yu, Z. Shen, Dislocation network in additive manufactured steel breaks strength–ductility trade-off, Mater. Today (2017).
[17] Y. Zhong, L. Liu, S. Wikman, D. Cui, Z. Shen, Intragranular cellular segregation network structure strengthening 316L stainless steel prepared by selective laser melting, J. Nucl. Mater. 470 (2016) 170-178.
[18] G. Nicoletto, Efficient determination of influence factors in fatigue of additive manufactured metals, Procedia Structural Integrity 8 (2018) 184-191.
[19] J. Smith, W. Xiong, W. Yan, S. Lin, P. Cheng, O.L. Kafka, G.J. Wagner, J. Cao, W.K. Liu, Linking process, structure, property, and performance for metal-based additive manufacturing: computational approaches with experimental support, Computational Mechanics 57(4) (2016) 583-610.
[20] Y. Kok, X. Tan, P. Wang, M. Nai, N. Loh, E. Liu, S. Tor, Anisotropy and heterogeneity of microstructure and mechanical properties in metal additive manufacturing: A critical review, Mater. Des. 139 (2018) 565-586.
[21] K.S. Chan, A microstructure-based fatigue-crack-initiation model, Metall. Mater. Trans. A 34(1) (2003) 43-58.
[22] K. Tanaka, T. Mura, A dislocation model for fatigue crack initiation, Journal of Applied Mechanics 48(1) (1981) 97-103.
[23] C.U. Brown, G. Jacob, M. Stoudt, S. Moylan, J. Slotwinski, A. Donmez, Interlaboratory study for nickel alloy 625 made by laser powder bed fusion to quantify mechanical property variability, J. Mater. Eng. Perform. 25(8) (2016) 3390-3397.
[24] S. Leuders, M. Vollmer, F. Brenne, T. Tröster, T. Niendorf, Fatigue strength prediction for titanium alloy TiAl6V4 manufactured by selective laser melting, Metall. Mater. Trans. A 46(9) (2015) 3816-3823.
[25] W. Yan, S. Lin, O.L. Kafka, Y. Lian, C. Yu, Z. Liu, J. Yan, S. Wolff, H. Wu, E. Ndip-Agbor, M. Mozaffar, K. Ehmann, J. Cao, G.J. Wagner, W.K. Liu, Data-driven multi-scale multi-physics models to derive process–structure–property relationships for additive manufacturing, Computational Mechanics 61(5) (2018) 521-541.
[26] Z. Hu, S. Mahadevan, Uncertainty quantification in prediction of material properties during additive manufacturing, Scripta Materialia 135 (2017) 135-140.

[27] M. Zhang, C.-N. Sun, X. Zhang, J. Wei, D. Hardacre, H. Li, Predictive models for fatigue property of laser powder bed fusion stainless steel 316L, Mater. Des. 145 (2018) 42-54.
[28] A.M. Aboutaleb, L. Bian, A. Elwany, N. Shamsaei, S.M. Thompson, G. Tapia, Accelerated process optimization for laser-based additive manufacturing by leveraging similar prior studies, IISE Transactions 49(1) (2017) 31-44.
[29] B. HKDH, Neural networks in materials science, ISIJ international 39(10) (1999) 966-979.
[30] G. Casalino, S.L. Campanelli, F. Memola Capece Minutolo, Neuro-fuzzy model for the prediction and classification of the fused zone levels of imperfections in Ti6Al4V alloy butt weld, Advances in Materials Science and Engineering 2013 (2013).
[31] S. Singh, H. Bhadeshia, D. MacKay, H. Carey, I. Martin, Neural network analysis of steel plate processing, Ironmaking and Steelmaking 25(5) (1998) 355-365.
[32] J.-S. Jang, ANFIS: adaptive-network-based fuzzy inference system, IEEE transactions on systems, man, and cybernetics 23(3) (1993) 665-685.
[33] L.A. Zadeh, Outline of a new approach to the analysis of complex systems and decision processes, IEEE Transactions on Systems, Man, and Cybernetics SMC-3(1) (1973) 28-44.
[34] L.A. Zadeh, Fuzzy sets, Information and Control 8(3) (1965) 338-353.
[35] M. Bowman, G. Nordmark, J.T. Yao, Fuzzy logic approach in metals fatigue, International Journal of Approximate Reasoning 1(2) (1987) 197-219.
[36] T.D. Righiniotis, M.K. Chryssanthopoulos, Probabilistic fatigue analysis under constant amplitude loading, Journal of Constructional Steel Research 59(7) (2003) 867-886.
[37] B. Sudret, P. Hornet, J.-M. Stephan, Z. Guede, M. Lemaire, Probabilistic assessment of fatigue life including statistical uncertainties in the SN curve, 17th international conference on structural mechanics in reactor technology, 2003.
[38] J. Schooling, M. Brown, P. Reed, An example of the use of neural computing techniques in materials science—the modelling of fatigue thresholds in Ni-base superalloys, Mater. Sci. Eng. A 260(1-2) (1999) 222-239.
[39] A.P. Vassilopoulos, R. Bedi, Adaptive neuro-fuzzy inference system in modelling fatigue life of multidirectional composite laminates, Computational Materials Science 43(4) (2008) 1086-1093.
[40] M. Jarrah, Y. Al-Assaf, H.E. Kadi, Neuro-fuzzy modeling of fatigue life prediction of unidirectional glass fiber/epoxy composite laminates, Journal of composite materials 36(6) (2002) 685-700.
[41] M. Zhang, C.-N. Sun, X. Zhang, P.C. Goh, J. Wei, D. Hardacre, H. Li, Fatigue and fracture behaviour of laser powder bed fusion stainless steel 316L: Influence of processing parameters, Mater. Sci. Eng. A 703 (2017) 251-261.

[42] M. Zhang, C.-N. Sun, X. Zhang, P.C. Goh, J. Wei, H. Li, D. Hardacre, Elucidating the relations between monotonic and fatigue properties of laser powder bed fusion stainless steel 316L, JOM 70(3) (2018) 390–395.
[43] M. Zhang, C.-N. Sun, X. Zhang, J. Wei, D. Hardacre, H. Li, High cycle fatigue and ratcheting interaction of laser powder bed fusion stainless steel 316L: Fracture behaviour and stress-based modelling, Int. J. Fatigue 121 (2019) 252-264.
[44] W. Shifeng, L. Shuai, W. Qingsong, C. Yan, Z. Sheng, S. Yusheng, Effect of molten pool boundaries on the mechanical properties of selective laser melting parts, J. Mater. Process. Technol. 214(11) (2014) 2660-2667.
[45] D. Wang, C. Song, Y. Yang, Y. Bai, Investigation of crystal growth mechanism during selective laser melting and mechanical property characterization of 316L stainless steel parts, Mater. Des. 100 (2016) 291-299.
[46] K. Saeidi, X. Gao, Y. Zhong, Z.J. Shen, Hardened austenite steel with columnar sub-grain structure formed by laser melting, Mater. Sci. Eng. A 625 (2015) 221-229.
[47] M.H. Yoo, A.H. King, Intergranular fracture by slip/grain boundary interaction, Metall. Trans. A 21(9) (1990) 2431-2436.
[48] Z. Zhang, Z. Wang, Dependence of intergranular fatigue cracking on the interactions of persistent slip bands with grain boundaries, Acta Mater. 51(2) (2003) 347-364.
[49] M. Pridantsev, F. Levin, Effect of manganese on the structure and properties of nonmagnetic stainless steels, Metal Science and Heat Treatment 7(12) (1966) 786-789.
[50] T. Mukherjee, J. Zuback, A. De, T. DebRoy, Printability of alloys for additive manufacturing, Scientific reports 6 (2016).
[51] K. Darvish, Z.W. Chen, T. Pasang, Reducing lack of fusion during selective laser melting of CoCrMo alloy: Effect of laser power on geometrical features of tracks, Mater. Des. 112 (2016) 357-366.
[52] J. Cherry, H. Davies, S. Mehmood, N. Lavery, S. Brown, J. Sienz, Investigation into the effect of process parameters on microstructural and physical properties of 316L stainless steel parts by selective laser melting, Int. J. Adv. Manuf. Technol. 76(5-8) (2015) 869-879.
[53] R. Hardin, C. Beckermann, Effect of porosity on deformation, damage, and fracture of cast steel, Metall. Mater. Trans. A 44(12) (2013) 5316-5332.
[54] R. Li, J. Liu, Y. Shi, M. Du, Z. Xie, 316L stainless steel with gradient porosity fabricated by selective laser melting, J. Mater. Eng. Perform. 19(5) (2010) 666-671.
[55] R.O. Ritchie, The conflicts between strength and toughness, Nature Materials 10 (2011) 817.
[56] J.A. Anderson, E. Rosenfeld, A. Pellionisz, Neurocomputing, MIT press1988.
[57] T. Takagi, M. Sugeno, Derivation of fuzzy control rules from human operator's control actions, IFAC Proceedings Volumes 16(13) (1983) 55-60.

[58] E. Kayacan, M.A. Khanesar, Chapter 2 - Fundamentals of Type-1 Fuzzy Logic Theory, in: E. Kayacan, M.A. Khanesar (Eds.), Fuzzy Neural Networks for Real Time Control Applications, Butterworth-Heinemann2016, pp. 13-24.
[59] F.-J. Chang, Y.-T. Chang, Adaptive neuro-fuzzy inference system for prediction of water level in reservoir, Advances in Water Resources 29(1) (2006) 1-10.
[60] P. Werbos, Beyond regression: New tools for prediction and analysis in the behavioral sciences, Ph. D. dissertation, Harvard University (1974).
[61] J.-S.R. Jang, Fuzzy modeling using generalized neural networks and kalman filter algorithm, AAAI, 1991, pp. 762-767.
[62] S.-K. Sin, R.J. de Figueiredo, Fuzzy system design through fuzzy clustering and optimal predefuzzification, [Proceedings 1993] Second IEEE International Conference on Fuzzy Systems, IEEE, 1993, pp. 190-195.
[63] S. Chopra, R. Mitra, V. Kumar, Identification of rules using subtractive clustering with application to fuzzy controllers, Machine Learning and Cybernetics, 2004. Proceedings of 2004 International Conference on, IEEE, 2004, pp. 4125-4130.
[64] S.L. Chiu, Fuzzy model identification based on cluster estimation, Journal of Intelligent & fuzzy systems 2(3) (1994) 267-278.
[65] G. Ciaburro, MATLAB for Machine Learning: Practical examples of regression, clustering and neural networks, Packt Publishing2017.
[66] M.F. Azeem, M. Hanmandlu, N. Ahmad, Structure identification of generalized adaptive neuro-fuzzy inference systems, IEEE Transactions on Fuzzy Systems 11(5) (2003) 666-681.
[67] A. Spierings, T. Starr, K. Wegener, Fatigue performance of additive manufactured metallic parts, Rapid Prototyping Journal 19(2) (2013) 88-94.
[68] S. Leuders, T. Lieneke, S. Lammers, T. Tröster, T. Niendorf, On the fatigue properties of metals manufactured by selective laser melting–The role of ductility, J. Mater. Res. 29(17) (2014) 1911-1919.
[69] T.M. Mower, M.J. Long, Mechanical behavior of additive manufactured, powder-bed laser-fused materials, Mater. Sci. Eng. A 651 (2016) 198-213.
[70] N. Dowling, C. Calhoun, A. Arcari, Mean stress effects in stress‐life fatigue and the Walker equation, Fatigue Fract. Eng. Mater. Struct. 32(3) (2009) 163-179.
[71] L. Prasad, Handbook of mechanical design, Tata McGraw-Hill Education1995.
[72] R. Molaei, A. Fatemi, N. Phan, Significance of hot isostatic pressing (HIP) on multiaxial deformation and fatigue behaviors of additive manufactured Ti-6Al-4V including build orientation and surface roughness effects, Int. J. Fatigue 117 (2018) 352-370.
[73] M.A. Bessa, R. Bostanabad, Z. Liu, A. Hu, D.W. Apley, C. Brinson, W. Chen, Wing K. Liu, A framework for data-driven analysis of materials under uncertainty: Countering the curse of dimensionality, Computer Methods in Applied Mechanics and Engineering 320 (2017) 633-667.

[74] K.S. Chan, Roles of microstructure in fatigue crack initiation, Int. J. Fatigue 32(9) (2010) 1428-1447.
[75] O.Y. Al-Jarrah, P.D. Yoo, S. Muhaidat, G.K. Karagiannidis, K. Taha, Efficient machine learning for big data: A review, Big Data Research 2(3) (2015) 87-93.